

RECYCLED



RECEIVED

MAR 07 2003

TECH CENTER 1600/2900

Exhibit 1

The Structure of the Potassium Channel: Molecular Basis of K^+ Conduction and Selectivity

Declan A. Doyle, João Morais Cabral, Richard A. Pfuetzner,
Anling Kuo, Jacqueline M. Gulbis, Steven L. Cohen,
Brian T. Chait, Roderick MacKinnon*

The potassium channel from *Streptomyces lividans* is an integral membrane protein with sequence similarity to all known K^+ channels, particularly in the pore region. X-ray analysis with data to 3.2 angstroms reveals that four identical subunits create an inverted teepee, or cone, cradling the selectivity filter of the pore in its outer end. The narrow selectivity filter is only 12 angstroms long, whereas the remainder of the pore is wider and lined with hydrophobic amino acids. A large water-filled cavity and helix dipoles are positioned so as to overcome electrostatic destabilization of an ion in the pore at the center of the bilayer. Main chain carbonyl oxygen atoms from the K^+ channel signature sequence line the selectivity filter, which is held open by structural constraints to coordinate K^+ ions but not smaller Na^+ ions. The selectivity filter contains two K^+ ions about 7.5 angstroms apart. This configuration promotes ion conduction by exploiting electrostatic repulsive forces to overcome attractive forces between K^+ ions and the selectivity filter. The architecture of the pore establishes the physical principles underlying selective K^+ conduction.

Potassium ions diffuse rapidly across cell membranes through proteins called K^+ channels. This movement underlies many fundamental biological processes, including electrical signaling in the nervous system. Potassium channels use diverse mechanisms of gating (the processes by which the pore opens and closes), but they all exhibit very similar ion permeability characteristics (1). All K^+ channels show a selectivity sequence of $K^+ \approx Rb^+ > Cs^+$, whereas permeability for the smallest alkali metal ions Na^+ and Li^+ is immeasurably low. Potassium is at least 10,000 times more permeant than Na^+ , a feature that is essential to the function of K^+ channels. Potassium channels also share a constellation of permeability characteristics that is indicative of a multi-ion conduction mechanism: The flux of ions in one direction shows high-order coupling to flux in the opposite direction, and ionic mixtures result in anomalous conduction behavior (2). Because of these

properties, K^+ channels are classified as "long pore channels," invoking the notion that multiple ions queue inside a long, narrow pore in single file. In addition, the pores of all K^+ channels can be blocked by tetraethylammonium (TEA) ions (3).

Molecular cloning and mutagenesis experiments have reinforced the conclusion that all K^+ channels have essentially the same pore constitution. Without exception, all contain a critical amino acid sequence, the K^+ channel signature sequence. Mutation of these amino acids disrupts the channel's ability to discriminate between K^+ and Na^+ ions (4).

Two aspects of ion conduction by K^+ channels have tantalized biophysicists for the past quarter century. First, what is the chemical basis of the impressive fidelity with which the channel distinguishes between K^+ and Na^+ ions, which are featureless spheres of Pauling radius 1.33 Å and 0.95 Å, respectively? Second, how can K^+ channels be so highly selective and at the same time, apparently paradoxically, exhibit a throughput rate approaching the diffusion limit? The 10^4 margin by which K^+ is selected over Na^+ implies strong energetic interactions between K^+ ions and the pore. And yet strong energetic interactions seem incongruent with throughput rates up to 10^8 ions per second. How can these two essential features of the K^+ channel pore be reconciled?

Potassium Channel Architecture

The amino acid sequence of the K^+ channel from *Streptomyces lividans* (KcsA K^+ channel) (5) is similar to that of other K^+ channels, including vertebrate and invertebrate voltage-dependent K^+ channels, vertebrate inward rectifier and Ca^{2+} -activated K^+ channels, K^+ channels from plants and bacteria, and cyclic nucleotide-gated cation channels (Fig. 1). On the basis of hydrophobicity analysis, there are two closely related varieties of K^+ channels, those containing two membrane-spanning segments per subunit and those containing six. In all cases, the functional K^+ channel protein is a tetramer (6), typically of four identical subunits (7). Subunits of the two membrane-spanning variety appear to be shortened versions of their larger counterparts, as if they simply lack the first four membrane-spanning segments. Although the KcsA K^+ channel is a two membrane-spanning K^+ channel, its amino acid sequence is actually closer to those of eukaryotic six membrane-spanning K^+ channels. In particular, its sequence in the pore region, located between the membrane-spanning stretches and containing the K^+ channel signature sequence, is nearly identical to that found in the *Drosophila* (Shaker) and vertebrate voltage-gated K^+ channels (Fig. 1). In an accompanying paper, through a study of the KcsA K^+ channel interaction with eukaryotic K^+ channel toxins, we confirm that the KcsA pore structure is indeed very similar to that of eukaryotic K^+ channels and that its structure is maintained when it is removed from the membrane with detergent (8).

We have determined the KcsA K^+ channel structure from residue position 23 to 119 by x-ray crystallography (Table 1). The cytoplasmic carboxyl terminus (residues 126 to 158) was removed in the preparation and the remaining residues were disordered. The KcsA K^+ channel crystals are radiation-sensitive and the diffraction pattern is anisotropic, with reflections observed along the best and worst directions at 2.5 Å and 3.5 Å Bragg spacings, respectively. By data selection, anisotropy correction, introduction of heavy atom sites by site-directed mutagenesis, averaging, and solvent flattening, an interpretable electron density map was calculated (Fig. 2, A through C). This map was without main chain breaks and showed strong side chain density (Fig. 2C). The model was refined with data to 3.2 Å (the data set was 93 % complete to 3.2 Å with 67% completeness between 3.3 Å and 3.2 Å), maintaining highly restrained stereochemistry and keeping tight noncrystallographic symmetry restraints. The refinement procedure was

D. A. Doyle, R. A. Pfuetzner, A. Kuo, and R. MacKinnon are in the Laboratory of Molecular Neurobiology and Biophysics and the Howard Hughes Medical Institute, Rockefeller University, 1230 York Avenue, New York, NY 10021, USA. J. M. Cabral and J. M. Gulbis are in the Laboratory of Molecular Neurobiology and Biophysics, Rockefeller University, 1230 York Avenue, New York, NY 10021, USA. S. L. Cohen and B. T. Chait are in the Laboratory of Mass Spectrometry and Gaseous Ion Chemistry, Rockefeller University, 1230 York Avenue, New York, NY 10021, USA.

*To whom correspondence should be addressed. E-mail: mackinn@rockvax.rockefeller.edu

monitored by minimizing the value R -free (29.0%) and its separation from R -crystallographic (28.0%). The presence of four molecules (subunits) in the asymmetric unit of the crystal provides a very significant enhancement of the accuracy of the crystallographic analysis; first, by enabling averaging of the electron density over four crystallographically independent regions of the multiple isomorphous replacement (MIR) map, and second, by providing a powerful set of constraints on the atomic model during refinement (9).

The K^+ channel is a tetramer with four-fold symmetry about a central pore (Fig. 3, A and B). Like several other membrane proteins, it has two layers of aromatic amino acids positioned to extend into the lipid bilayer, presumably near the membrane-water interfaces (Fig. 3C) (10). Each subunit has two transmembrane α -helices connected by the roughly 30 amino acid pore region, which consists of the turret, pore helix, and selectivity filter (Fig. 3, A and B). A subunit is inserted into the tetramer such that one transmembrane helix (inner helix) faces the central pore while the other (outer helix) faces the lipid membrane. The inner helices are tilted with respect to the mem-

brane normal by about 25° and are slightly kinked, so that the subunits open like the petals of a flower facing the outside of the cell. The open petals house the structure formed by the pore region near the extracellular surface of the membrane. This region contains the K^+ channel signature sequence, which forms the selectivity filter (4). The essential features of subunit packing can be appreciated by viewing the relation between the four inner helices and the four pore helices (Fig. 3D). The four inner helices pack against each other as a bundle near the intracellular aspect of the membrane, giving the appearance of an inverted teepee. The pore helices are slotted in between the poles of the teepee and are directed, with an amino-to-carboxyl sense, toward a point near the center of the channel (Fig. 3, A, B, and D). This pore helix arrangement provides many of the intersubunit contacts that hold the tetramer together and, as discussed below, is also critical in the operation of the ion conduction pore.

Sequence conservation among K^+ channels (including ones with two and six membrane-spanning segments), as well as cyclic nucleotide-gated cation channels, is strongest for the amino acids corresponding to

the pore region and the inner helix. Even Na^+ and Ca^{2+} channels show distant relatedness over these segments. The teepee architecture of the K^+ channel pore likely will be a general feature of all of these cation channels, with four inner helices arranged like the poles of a teepee, four pore helices, and a selectivity filter—tuned to select the appropriate cation—located close to the extracellular surface.

This structure of the KcsA K^+ channel is in excellent agreement with results from functional and mutagenesis studies on Shaker and other eukaryotic K^+ channels (Fig. 4). The pore-region of K^+ channels was first defined with pore-blocking scorpion toxins (11). These inhibitors interact with amino acids (Fig. 4, white) comprising the broad extracellular-facing entryway to the pore (12). The impermeant organic cation TEA blocks K^+ channels from both sides of the membrane at distinct sites (13). Amino acids interacting with externally and internally applied TEA are located just external to (Fig. 4, yellow) and internal to (Fig. 4, mustard) the structure formed by the signature sequence amino acids (14, 15). Alteration of the signature sequence amino acids (Fig. 4, red main chain atoms) disrupts K^+ selectivity (4). Amino acids close to the intracellular opening on the Shaker K^+ channel map to the inner helix on the KcsA K^+ channel (16). Interestingly, exposure to the cytoplasm of the region above the inner helix bundle (Fig. 4, pink side chains) requires an open voltage-dependent gate, whereas the region at or below the bundle (Fig. 4, green side chains) is exposed whether or not the gate was open. The correlation between the transition zone for gate-dependent exposure to the cytoplasm in the Shaker K^+ channel and the inner helix bundle in this structure has implications for mechanisms of gating in K^+ channels.

General Properties of the Ion Conduction Pore

As might have been anticipated for a cation channel, both the intracellular and extracellular entryways are negatively charged by acidic amino acids (Fig. 5A, red), an effect that would raise the local concentration of cations while lowering the concentration of anions. The overall length of the pore is 45 Å, and its diameter varies along its distance (Fig. 5B). From inside the cell (bottom) the pore begins as a tunnel 18 Å in length (the internal pore) and then opens into a wide cavity (~10 Å across) near the middle of the membrane. A K^+ ion could move throughout the internal pore and cavity and still remain mostly hydrated. In contrast, the selectivity filter separating the cavity

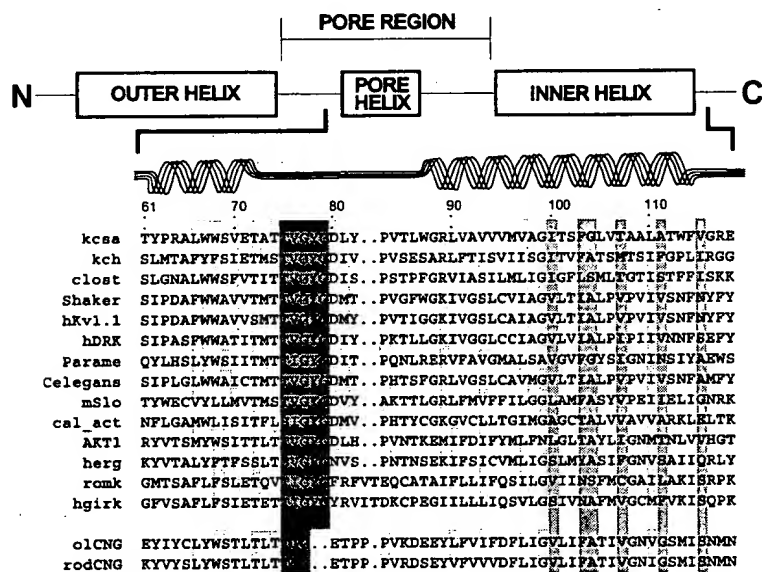
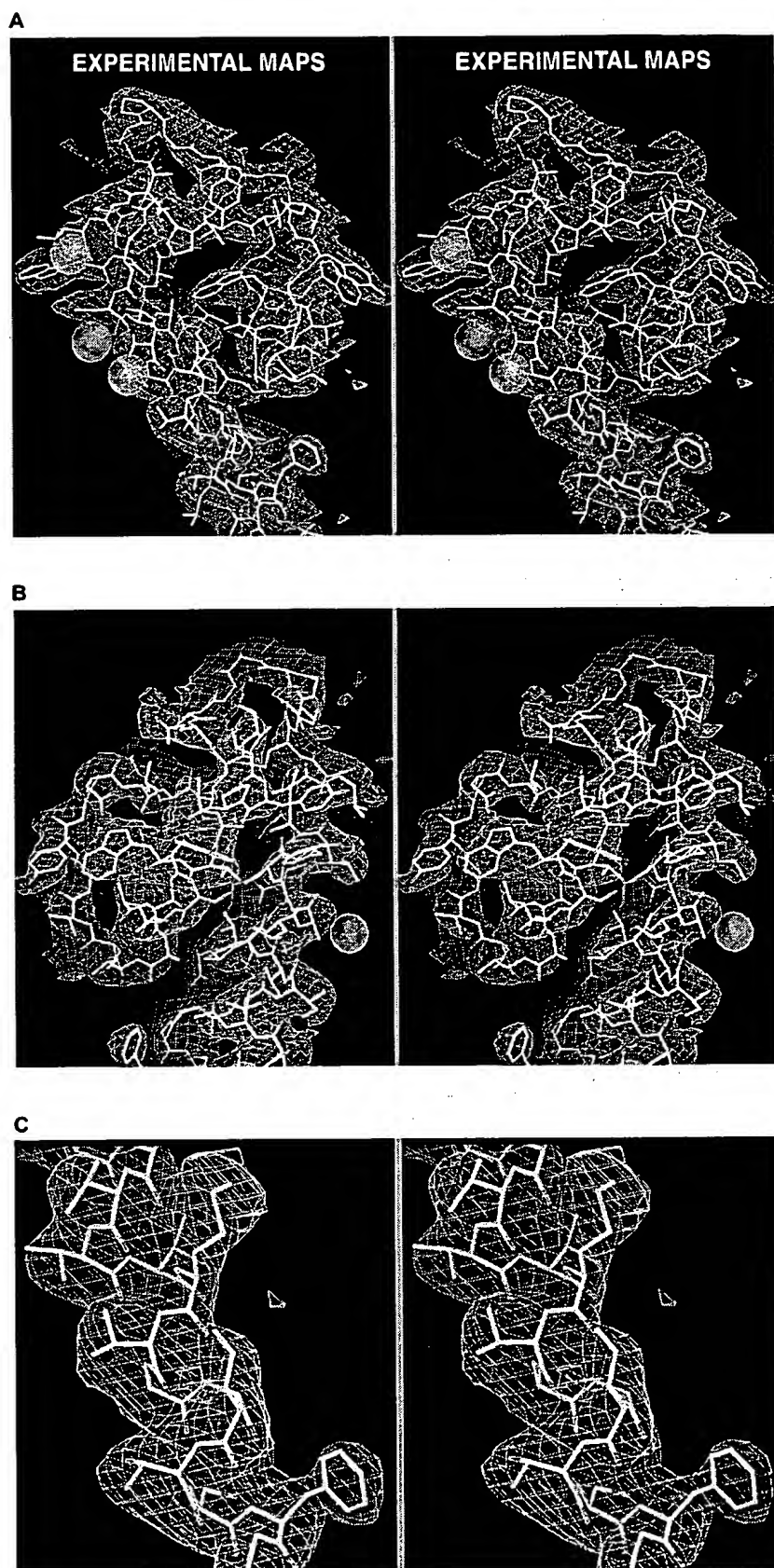


Fig. 1. Sequence alignment of selected K^+ channels and cyclic nucleotide-gated channels. The numbering and secondary structural elements for the *Streptomyces lividans* K^+ channel (KcsA) is given above the sequences. Selectivity filter, red; lining of the cavity and inner pore, blue; residues in which the nature of the side chain is preserved (>50% similarity), grey. The sequences are: KcsA, *Streptomyces lividans*, accession number (acc) PIR S60172; kch, *Escherichia coli*, acc GenBank U24203; clost, *Clostridium acetobutylicum* (Genome Therapeutics Corp.); Shaker, *Drosophila melanogaster*, acc PIR S00479; hKv1.1, *Homo sapiens*, acc Swissprot Q09470; hDRK, *H. sapiens*, acc PIR S31761; Parame, *Paramecium tetraurelia*, acc GenBank U19908; C elegans, *Caenorhabditis elegans*, acc GenBank AF005246; mSlo, *Mus musculus*, acc PIR A48206; cal_act, *H. sapiens*, acc GenBank AF031815; AKT1, *Arabidopsis thaliana*, acc PIR S62694; herg, *H. sapiens*, acc PIR I38465; romk, *Rattus norvegicus*, acc Swissprot P35560; hgrk, *H. sapiens*, acc GenBank S78684; oCNG, *H. sapiens*, acc Swissprot Q16280; rodCNG, *H. sapiens*, acc PIR A42161. The last two sequences, separate from the rest, are from cyclic nucleotide-gated channels, which are not K^+ selective.

from the extracellular solution is so narrow that a K^+ ion would have to shed its hydrating waters to enter. The chemical composition of the wall lining the internal pore and cavity is predominantly hydrophobic (Fig. 5A, yellow). The selectivity filter, on the other hand, is lined exclusively by polar main chain atoms belonging to the signature sequence amino acids. The distinct mechanisms operating in the cavity and internal pore versus the selectivity filter will be discussed below, but first we introduce the determination of K^+ ion positions in the pore.

Potassium channels exclude the smaller alkali metal cations Li^+ (radius 0.60 Å) and Na^+ (0.95 Å) but allow permeation of the larger members of the series Rb^+ (1.48 Å) and Cs^+ (1.69 Å). In fact, Rb^+ is nearly a perfect K^+ (1.33 Å) analog because its size and permeability characteristics are very similar to those of K^+ . Because they are more electron dense than K^+ , Rb^+ and Cs^+ allow visualization of the locations of permeant ions in the pore. By difference electron density maps calculated with data from crystals transferred into Rb^+ -containing (Fig. 6a) or Cs^+ -containing (Fig. 6b) solutions, multiple ions are well defined in the pore. The selectivity filter contains two ions (inner and outer ions) located at opposite ends, about 7.5 Å apart (center to center). In the Rb^+ difference map, there actually are two partially separated peaks at the inner aspect of the selectivity filter. These peaks are too close to each other (2.6 Å) to represent two simultaneously occupied ion binding sites. We suspect that they represent a single ion (on average) in rapid equilibrium between adjacent sites. The single inner ion peak in the Cs^+ difference map undoubtedly reflects the lower resolution at which the map was calculated (to 5 Å for Cs^+ versus 4.0 Å for Rb^+), because the Rb^+ difference map, when calculated at the same lower resolution, also shows only a single peak at the Cs^+ position. The Rb^+ positions correspond to strong peaks (pre-

Fig. 2. Experimental electron density map. Stereoviews of the experimental electron-density map contoured at 1σ covering nearly an entire subunit (removed from the tetramer) of the final model. The map was calculated at 3.2 Å resolution with the following Fourier coefficients: native-sharpened amplitudes and MIR solvent flattened averaged phases. (A) Foreground: map showing inner helix, loop structures and selectivity filter; background: the pore helix and outer helix. CPK spheres show positions of mercury atoms used as residue markers (from the top, marked residues are Leu⁶⁶, Leu⁹⁰ and Val⁹³). (B) Alternative view. Foreground: pore helix and part of outer helix; background: selectivity filter and turret. CPK sphere marks position of Ala⁴². (C) Close up view of electron density.



sumably, K⁺ ions) in a high contour native electron density map (not shown). Thus, the selectivity filter contains two K⁺ ions. A third weaker peak is located below the selectivity filter at the center of the large cavity in the Rb⁺ difference map (Fig. 6a, cavity ion) and in the Cs⁺ difference map at a lower contour (not shown). Electron density at the cavity center is prominent in MIR maps, even prior to averaging (Fig. 6c,

lower diffuse peak). The difference electron density maps show this to be related to the presence of one or more poorly localized cations situated at least 4 Å away from the closest protein groups.

The Cavity and Internal Pore

Why is there a 10 Å diameter cavity in the center of the channel with an ion in it

(Fig. 5B and Fig. 6)? Electrostatic calculations show that when an ion is moved along a narrow pore through a membrane, it must cross an energy barrier that is maximum at the membrane center (17). The electrostatic field emanating from a cation polarizes its environment, bringing the negative ends of dipoles closer to it and thereby stabilizing it. At the bilayer center, the polarizability of the surround-

Table 1. Summary of data collection and refinement statistics. Crystals (space group C2: $a = 128.8$ Å, $b = 68.9$ Å, $c = 112.0$ Å, $\beta = 124.6^\circ$) were flash-frozen by being transferred directly from the crystal mother liquor to a stream of boiled-off nitrogen (24). Because crystals of the mutant L90C diffracted significantly better than wild-type protein crystals, the former were used for native data collection. Data were collected from multiple crystals, and six sets were selected and merged to form the native data set used for structure determination. Mercury derivatives were obtained by direct addition of methyl mercury to the crystallization solution of cysteine mutant crystals. MALDI-TOF mass spectrometry confirmed 60 to 90% derivatization of crystals prior to data collection. All data were collected at Cornell High Energy Synchrotron Source (CHESS), station A1, with the Princeton 2K CCD (25). Data were processed with DENZO and SCALEPACK (26) and the CCP4 package (27). Heavy atom positions were determined with SHELX-97 (28) and cross-difference Fourier analysis. These positions confirmed the fourfold noncrystallographic symmetry observed in the self-rotation Patterson function and allowed the determination of initial orientation matrices. An initial model (90% complete) was built into a solvent flattened (64% solvent content), fourfold averaged electron density map with the program O (29). The tracing of the model was facilitated by the use of the mercury atom positions as residue markers. L86C was used solely for this purpose. After torsional

refinement (with strict fourfold noncrystallographic symmetry constraints) with X-PLOR 3.851 (30), this model was used in the anisotropic scaling [sharpening (31)] of the native data with X-PLOR. The structure factor sigma values were also rescaled appropriately, and the corrected data were used for all subsequent procedures. Fourfold averaging, solvent flattening, and phase extension were applied in DM (32), resulting in a marked improvement of the electron density that allowed correction of the model and the building of additional residues. Refinement consisted of rounds of positional (in the initial stages phase information was also included as a restraint) and grouped *B*-factor refinement in X-PLOR. Fourfold noncrystallographic symmetry was highly restrained with the force constant for positional restraints set as 1000 kcal/mol/Å². The diffuse ion cloud described in the text was initially modeled as one or more K⁺ ions and several water molecules; however, the results were unsatisfactory. Therefore, this and other strong unmodelled density present in solvent-flattened maps (no averaging included) was Fourier back-transformed, scaled, and included in the refinement procedure as partial structure factors. The final model includes amino acids 23 to 119 of each chain. The following residues were truncated: Arg²⁷ to C β , Ile⁶⁰ to C γ , Arg⁶⁴ to C β , Glu⁷¹ to C β , and Arg¹¹⁷ to N ϵ . The stereochemistry is strongly restrained, with no outliers on the Ramachandran plot. The high *B*-factor values reflect the intensity decay of the data beyond 4 Å.

| Data collection and phasing | | | | | | |
|-----------------------------|----------------|------------|--------------------------------|----------------------|---------------------|---|
| Data set | Resolution (Å) | Redundancy | Completeness overall/outer (%) | R_{merge}^* | Phasing power† | <i>R</i> -Cullis‡ |
| L90C-a | 15.0–3.7 | 3.5 | 91.3/93.3 | 0.071 | 1.61 | 0.70 |
| L90C-b | 15.0–3.7 | 7.0 | 91.5/94.1 | 0.083 | 1.87 | 0.50 |
| V93C | 15.0–3.7 | 4.1 | 98.3/99.1 | 0.075 | 1.35 | 0.63 |
| A32C | 15.0–4.0 | 2.3 | 84.1/83.8 | 0.076 | 1.45 | 0.66 |
| A29C | 15.0–5.0 | 2.7 | 73.9/74.0 | 0.063 | 1.03 | 0.85 |
| A42C | 15.0–6.5 | 2.0 | 90.7/90.3 | 0.057 | 0.97 | 0.81 |
| L86C | 30.0–6.0 | 2.3 | 58.7/58.9 | 0.057 | — | — |
| | | | | | <i>I</i> / σ | % of measured data with <i>I</i> / σ > 2 |
| Native | 30.0–3.2 | 6.1 | 93.3% | 0.086 | 15.8 | 75 |
| Outer Shell | 3.3–3.2 | 2.3 | 66.6% | 0.286 | 3.9 | 50 |

| Anisotropic correction | | |
|------------------------|------------------------------|-----------------------------|
| | Average F.O.M (30.0–3.2 Å) | Average F.O.M (3.4–3.2 Å) |
| Before sharpening¶ | 0.76 | 0.55 |
| After sharpening¶ | 0.83 | 0.64 |

| Refinement | | Root-mean-square deviation of | |
|---|--------------------------------|---|-------------------|
| Resolution: | 10.0–3.2 Å | Bond angles: | 1.096° |
| R-cryst.§: | 28.0% | Bond lengths: | 0.005 Å |
| R-free§: | 29.0% | Ncs related atoms: | 0.006 Å |
| No. of reflections with $ F /\sigma F > 2$: | 12054 | <i>B</i> -factor for ncs related atoms: | 10 Å ² |
| No. of protein atoms: | 710 per subunit | <i>B</i> -factor for non-bonded atoms: | 36 Å ² |
| No. of ligand atoms: | 1 water, 3 K ⁺ ions | | |
| Mean <i>B</i> -factor for main-chain atoms: | 90 Å ² | | |
| Mean <i>B</i> -factor for side-chain atoms: | 110 Å ² | | |

* $R_{\text{merge}} = \sum \sum |I - \langle I \rangle| / \sum I$. †Phasing power = $(\langle |F_n| \rangle) / (E)$. ‡*R*-Cullis = $\sum |F_p - F_{\text{calc}}| - |F_{\text{nc}}| / \sum |F_p - F_{\text{calc}}|$, only for centric data. §*R*-cryst. = $\sum |F_p - F_{\text{calc}}| / \sum |F_p|$, *R*-free the same as *R*-cryst, but calculated on 10% of data selected in thin resolution shells and excluded from refinement. ||Figure of merit. ¶In both cases, fourfold averaging and solvent flattening were applied; I is the observed intensity, $\langle I \rangle$ is the average intensity, F_n is the root-mean-square heavy-atom structure factor, E is the lack of closure error, F_p is the structure factor for the derivative, F_{nc} is the structure factor for the native, F_{calc} is the calculated structure factor for the heavy atom, and F_{calc} is the calculated native structure factor.

ing medium is minimal and therefore the energy of the cation is highest. Thus, simple electrostatic considerations allow us to

understand the functional significance of the cavity and its strategic location. The cavity overcomes the electrostatic desta-

bilization resulting from the low dielectric bilayer by simply surrounding an ion with polarizable water. A second feature of the K^+ channel structure also stabilizes a cation at the bilayer center. The four pore helices point directly at the center of the cavity (Fig. 3, A, B, and D). The amino to carboxyl orientation of these helices will impose a negative electrostatic (cation attractive) potential via the helix dipole effect (18). The ends of the helices are rather far (~ 8 Å) from the cavity center, but all four contribute to the effect. Therefore, two properties of the structure, the aqueous cavity and the oriented helices, help to solve a fundamental physical problem in biology—how to lower the electrostatic barrier facing a cation crossing a lipid bilayer. Thus, the diffuse electron density in the cavity center (Fig. 6C) likely reflects a hydrated cation cloud rather than an ion binding site (Fig. 7).

Alternatively, the channel could have overcome the destabilizing electrostatic effects of the bilayer center by lining the entire pore with a polarizable surface, putting ion binding sites along its entire length. But the structure shows that, with the exception of the selectivity filter, the pore lining is mainly hydrophobic, a general property of K^+ channels (Fig. 1). This conclusion was anticipated by the landmark experiments of Armstrong, which showed that hydrophobic cations bind in

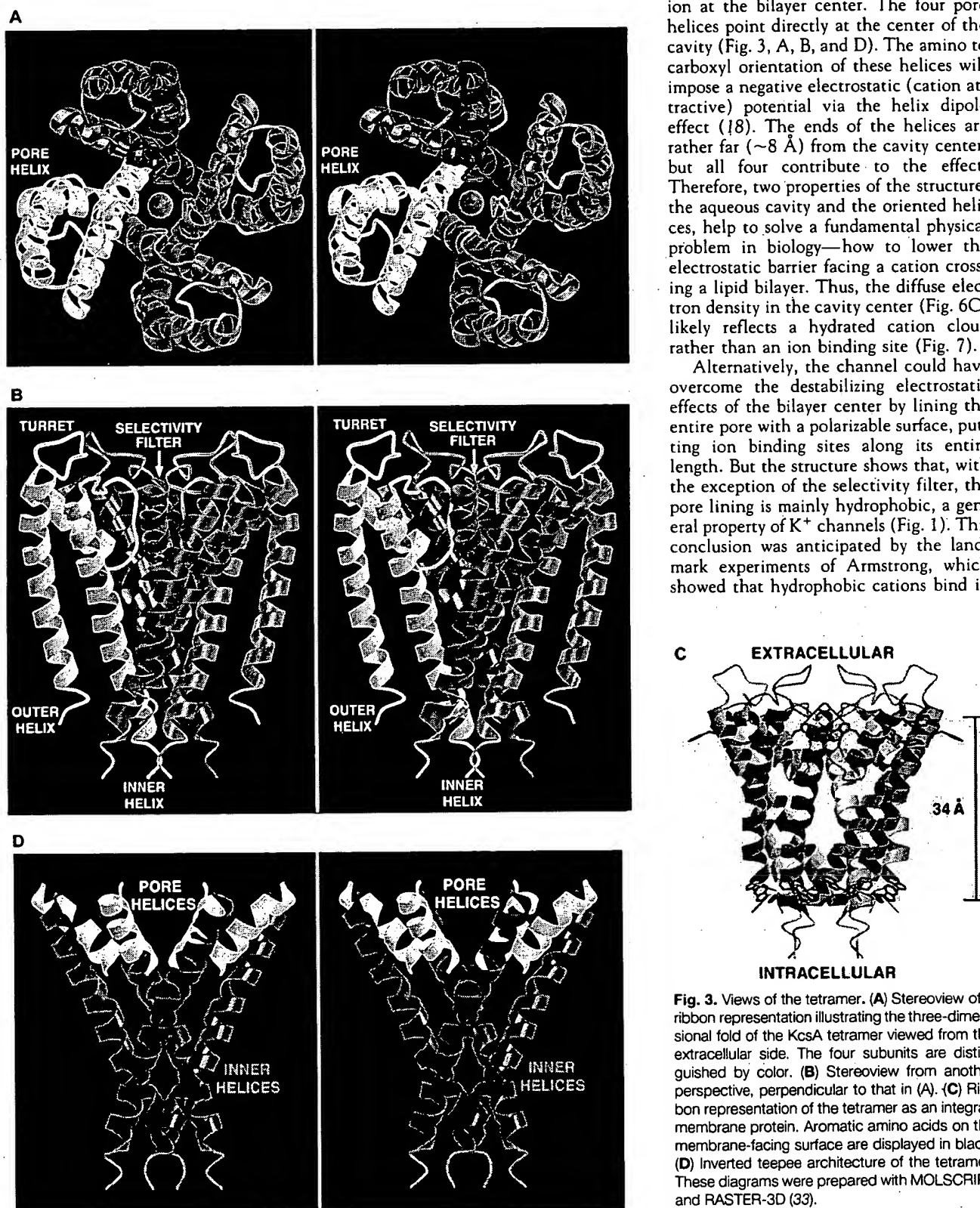


Fig. 3. Views of the tetramer. (A) Stereoview of a ribbon representation illustrating the three-dimensional fold of the KcsA tetramer viewed from the extracellular side. The four subunits are distinguished by color. (B) Stereoview from another perspective, perpendicular to that in (A). (C) Ribbon representation of the tetramer as an integral-membrane protein. Aromatic amino acids on the membrane-facing surface are displayed in black. (D) Inverted teepee architecture of the tetramer. These diagrams were prepared with MOLSCRIPT and RASTER-3D (33).

the pore of K⁺ channels (3). What is the significance of the hydrophobic lining? We suggest that it would be counterproductive to achieving a high throughput of K⁺ ions were the lining of the channel to interact strongly with ions outside of the selectivity filter. The hydrophobic lining presents a relatively inert surface to a diffusing ion over most of the length of the pore.

In summary, the inner pore and cavity lower electrostatic barriers without creating deep energy wells. The structural and chemical design of this part of the pore ensure a low resistance pathway from the cytoplasm to the selectivity filter, facili-

tating a high throughput. Functional experiments on K⁺ channels support this conclusion. When TEA from the cytoplasm migrates to its binding site at the top of the cavity (>50% of the physical distance across the membrane (Figs. 4 and 5)), it traverses only about 20% of the transmembrane voltage difference (15). Thus, 80% of the transmembrane voltage is imposed across the relatively short selectivity filter. The rate limiting steps for a K⁺ ion traversing the channel are thereby limited to this short distance. In effect, the K⁺ channel has thinned the relevant transmembrane diffusion distance to a mere 12 Å.

The Selectivity Filter

The atomic model for the K⁺ channel selectivity filter was based on the experimental electron density map, which showed a continuous ridge of electron density attributable to the main chain, as well as strong Val and Tyr side chain density directed away from the pore (Fig. 8A). We also used K⁺ ion positions defined by difference Fourier analysis (Figs. 6 and 8A, yellow density) and our knowledge of alkali metal cation coordination in small molecules. The side chain locations preclude their direct participation in ion coordination, leaving this function to the

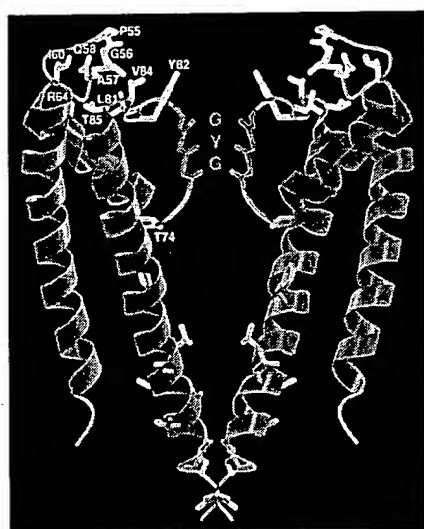
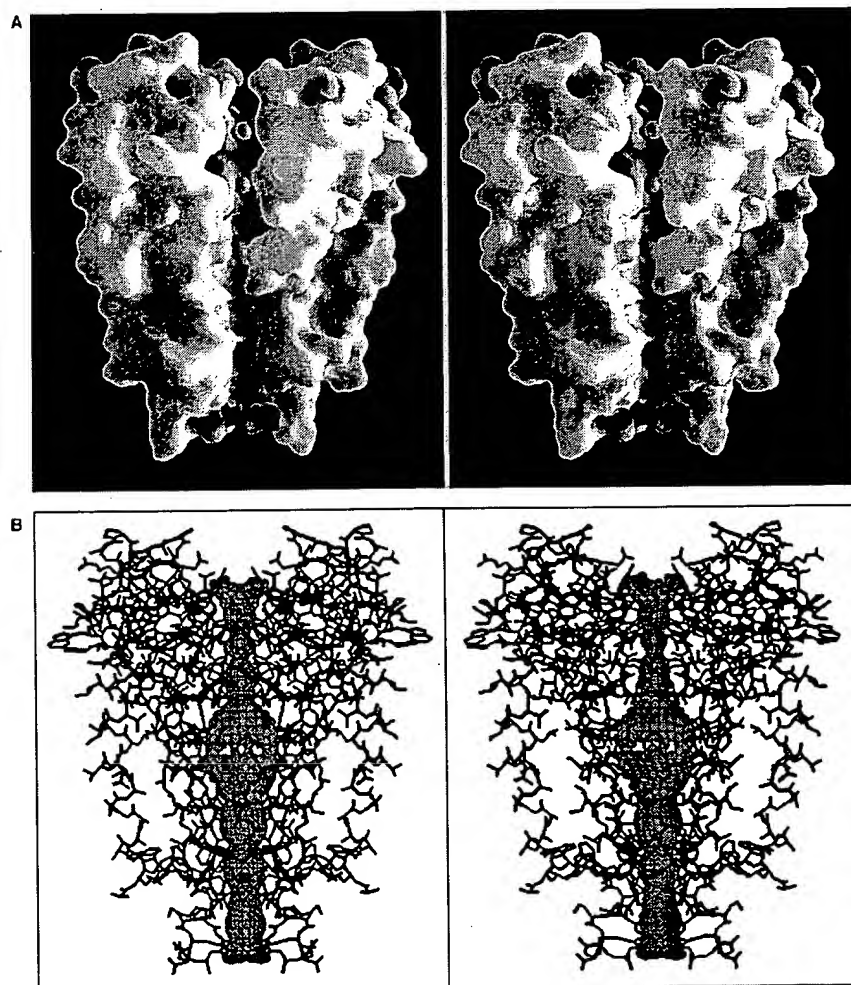


Fig. 4 (above). Mutagenesis studies on *Shaker*. Mapping onto the KcsA structure. Mutations in the voltage-gated *Shaker* K⁺ channel that affect function are mapped to the equivalent positions in KcsA based on the sequence alignment. Two subunits of KcsA are shown. Mutation of any of the white side chains significantly alters the affinity of agitoxin2 or charybdotoxin for the *Shaker* K⁺ channel (12). Changing the yellow side chain affects both agitoxin2 and TEA binding from the extracellular solution (14). This residue is the external TEA site. The mustard-colored side chain at the base of the selectivity filter affects TEA binding from the intracellular solution [the internal TEA site (15)]. The side chains colored green, when mutated to cysteine, are modified by cysteine-reactive agents whether or not the channel gate is open, whereas those colored pink react only when the channel is open (16). Finally, the residues colored red (GYG, main chain only) are absolutely required for K⁺ selectivity (4). This figure was prepared with MOLSCRIPT and RAS-TER-3D. **Fig. 5 (right).** Molecular surface of KcsA and contour of the pore. (A) A cutaway stereoview displaying the solvent-accessible surface of the K⁺ channel colored according to physical properties. Electrostatic potential was calculated with the program GRASP, assuming an ionic strength equivalent to 150 mM KCl and dielectric constants of 2 and 80 for protein and solvent, respectively. Side chains of Lys, Arg, Glu, and Asp residues were assigned single positive or negative charges as appropriate, and the surface coloration varies smoothly from blue in areas of high positive charge through white to



red in negatively charged regions. The yellow areas of the surface are colored according to carbon atoms of the hydrophobic (or partly so) side chains of several semi-conserved residues in the inner vestibule (Thr⁷⁵, Ile¹⁰⁰, Phe¹⁰³, Thr¹⁰⁷, Ala¹⁰⁸, Ala¹¹¹, Val¹¹⁵). The green CPK spheres represent K⁺ ion positions in the conduction pathway. (B) Stereoview of the entire internal pore. Within a stick model of the channel structure is a three-dimensional representation of the minimum radial distance from the center of the channel pore to the nearest van der Waals protein contact. The display was created with the program HOLE (34).

main chain atoms. The precise orientation of individual carbonyl oxygens cannot be discerned at the resolution of this x-ray analysis, but we propose that they are directed inward to account for K^+ ion coordination (Fig. 8B). A single water molecule (the only one modeled in the structure) located between the two K^+ ions in the selectivity filter was justified by the presence of a strong electron density peak in the experimental map, which was never associated with an ion peak in the difference Fourier maps (19).

The structure of the selectivity filter exhibits two essential features. First, the main chain atoms create a stack of sequential oxygen rings and thus afford numerous closely spaced sites of suitable dimensions for coordinating a dehydrated K^+ ion. The K^+ ion thus has only a very small distance to diffuse from one site to the next within the selectivity filter. The second important structural feature of the selectivity filter is the protein packing around it. The Val and Tyr side chains from the V-G-Y-G sequence point away from the pore and make

specific interactions with amino acids from the tilted pore helix. Together with the pore helix Trp residues, the four Tyr side chains form a massive sheet of aromatic amino acids, twelve in total, that is positioned like a cuff around the selectivity filter (Fig. 8C). The hydrogen bonding, for example between the Tyr hydroxyls and Trp nitrogens, and the extensive van der Waals contacts within the sheet, offer the immediate impression that this structure behaves like a layer of springs stretched radially outward to hold the pore open at its proper diameter.

How does the K^+ channel structure account for its prodigious ion selective properties? When an ion enters the selectivity filter, it evidently dehydrates (nearly completely). To compensate for the energetic cost of dehydration, the carbonyl oxygen atoms must take the place of the water oxygen atoms, come in very close contact with the ion, and act like surrogate water (20, 21). The structure reveals that the selectivity filter is held open as if to prevent it from accommodating a Na^+

ion with its smaller radius. We propose that a K^+ ion fits in the filter precisely so that the energetic costs and gains are well balanced. The structure of the selectivity filter with its molecular springs holding it open prevents the carbonyl oxygen atoms from approaching close enough to compensate for the cost of dehydration of a Na^+ ion.

In about 150 mM K^+ , the selectivity filter contains two K^+ ions (Figs. 6 and 8). The ions are located at opposite ends of the selectivity filter, separated by about 7.5 Å, roughly the average distance between K^+ ions in a 4 M KCl solution, and in the selectivity filter there are no intervening Cl^- anions to balance the charge. We therefore conclude that the selectivity filter attracts and concentrates K^+ ions. But how does such a selectivity filter ever conduct ions? The structure implies that a single K^+ ion would be held very tightly, but that the presence of two K^+ ions results in mutual repulsion, hence their locations near opposite ends of the selectivity filter. Thus, when a second ion enters, the attractive force between a K^+ ion and the selectivity filter becomes perfectly balanced by the repulsive force between ions, and this is what allows conduction to occur. This picture accounts for both a strong interaction between K^+ ions and the selectivity filter and a high throughput mediated by electrostatic repulsion. On the basis of functional measurements, the same concept of destabilization by multiple ion occupancy has been proposed for Ca^{2+} channels (22) and for K^+ channels (23) and may be a general property of all selective ion channels.

Summary

We propose that the following principles underlie the structure and operation of K^+ channels. (i) The pore is constructed of an inverted teepee, with the selectivity filter held at its wide end. This architecture also describes the pore of cyclic nucleotide-gated channels and probably Na^+ and Ca^{2+} channels as well. (ii) The narrow selectivity filter is only 12 Å long, whereas the remainder of the pore is wider and has a relatively inert hydrophobic lining. These structural and chemical properties favor a high K^+ throughput by minimizing the distance over which K^+ interacts strongly with the channel. (iii) A large water-filled cavity and helix dipoles help to overcome the high electrostatic energy barrier facing a cation in the low dielectric membrane center. (iv) The K^+ selectivity filter is lined by carbonyl oxygen atoms, which provide multiple closely spaced sites. The filter is constrained in an opti-

Fig. 6. Identification of permeant ion positions in the pore. (a) A Rb^+ difference Fourier map calculated to 4.0 Å and contoured at 6 σ identifies two strong peaks corresponding to ions in the selectivity filter (inner and outer ions) and a weaker peak corresponding to ions in the cavity (cavity ion). The inner ion density has two closely spaced peaks. (b) A Cs^+ difference Fourier map calculated to 5.0 Å and contoured at 6 σ shows the inner and outer ion peaks in the selectivity filter. Both difference Fourier maps were calculated with Fourier coefficients: $F(\text{soak}) - F(\text{native-unsharpened})$ and MIR phases. (c) Electron density map contoured at 1 σ showing diffuse density at the cavity ion position. This map was calculated with the following Fourier coefficients: unsharpened native amplitudes and MIR solvent-flattened phases (no averaging information was included).

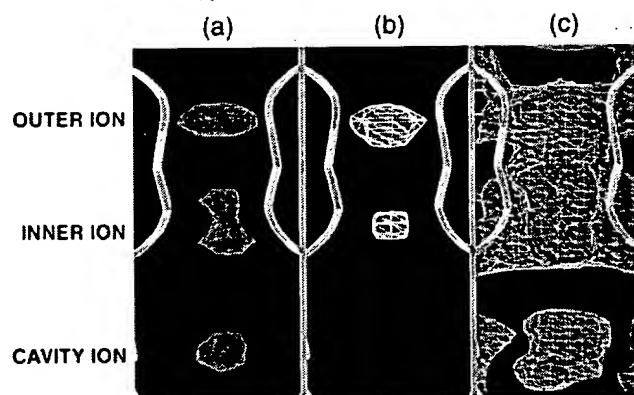
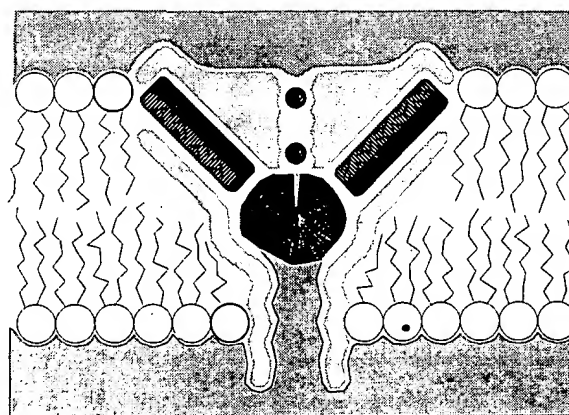


Fig. 7. Two mechanisms by which the K^+ channel stabilizes a cation in the middle of the membrane. First, a large aqueous cavity stabilizes an ion (green) in the otherwise hydrophobic membrane interior. Second, oriented helices point their partial negative charge (carboxyl end, red) towards the cavity where a cation is located.



mal geometry so that a dehydrated K^+ ion fits with proper coordination but the Na^+ ion is too small. (v) Two K^+ ions at close

proximity in the selectivity filter repel each other. The repulsion overcomes the otherwise strong interaction between ion

and protein and allows rapid conduction in the setting of high selectivity.

REFERENCES AND NOTES

1. B. Hille, *Ionic Channels of Excitable Membranes* (Sinauer, Sunderland, MA, ed. 2, 1992).
2. A. L. Hodgkin and R. D. Keynes, *J. Physiol. (London)* **128**, 61 (1955); S. Hagiwara, S. Miyazaki, S. Krasne, S. Ciani, *J. Gen. Physiol.* **70**, 269 (1977); B. Hille and W. Schwartz, *ibid.* **72**, 409 (1978); J. Neyton and C. Miller, *ibid.* **92**, 549 (1988).
3. C. M. Armstrong and L. Binstock, *J. Gen. Physiol.* **48**, 859 (1965); C. M. Armstrong, *ibid.* **50**, 491 (1966); *ibid.* **54**, 553 (1969); *ibid.* **58**, 413 (1971).
4. L. Heginbotham, T. Abramson, R. MacKinnon, *Science* **258**, 1152 (1992); L. Heginbotham, Z. Lu, T. Abramson, R. MacKinnon, *J. Biophys.* **66**, 1061 (1994).
5. H. Schempt et al., *EMBO J.* **14**, 5170 (1995); L. Heginbotham, E. Odessey, C. Miller, *Biochemistry* **36**, 10335 (1997); D. Marlen Cortes and E. Perozo, *ibid.*, p. 10343.
6. R. MacKinnon, *Nature* **350**, 232 (1991).
7. Certain K^+ channels contain the equivalent of two subunits in a single open reading frame. These are thought to form the tetramer through the assembly of two dimer subunits [K. A. Ketchum et al., *Nature* **376**, 690 (1995)].
8. R. MacKinnon et al., *Science* **280**, 106 (1998).
9. G. J. Kleywegt and R. J. Read, *Structure* **5**, 1557 (1998).
10. J. Deisenhofer et al., *Nature* **318**, 618 (1985); S. W. Cowan et al., *ibid.* **358**, 727 (1992); A. Kresch and G. E. Schulz, *J. Mol. Biol.* **243**, 891 (1994).
11. R. MacKinnon and C. Miller, *Science* **245**, 1382 (1989).
12. R. MacKinnon, L. Heginbotham, T. Abramson, *Neuron* **5**, 767 (1990); M. Stocker and C. Miller, *Proc. Natl. Acad. Sci. U.S.A.* **91**, 9509 (1994); S. A. N. Goldstein, D. J. Pheasant, C. Miller, *Neuron* **12**, 1377 (1994); P. Hidalgo and R. MacKinnon, *Science* **268**, 307 (1995); J. Ayar et al., *Neuron* **15**, 1169 (1995); D. Naranjo and C. Miller, *ibid.* **16**, 123 (1996); R. Ranganathan, J. H. Lewis, R. MacKinnon, *ibid.*, p. 131; A. Gross and R. MacKinnon, *ibid.*, p. 399.
13. C. M. Armstrong and B. Hille, *J. Gen. Physiol.* **59**, 388 (1972).
14. R. MacKinnon and G. Yellen, *Science* **250**, 276 (1990).
15. G. Yellen, M. E. Jurman, T. Abramson, R. MacKinnon, *ibid.* **251**, 939 (1991).
16. Y. Liu, M. Holmgren, M. E. Jurman, G. Yellen, *Neuron* **19**, 175 (1997).
17. V. A. Parsegian, *Ann. N.Y. Acad. Sci.* **264**, 161 (1975).
18. D. Sali, M. Bycroft, A. R. Fersht, *Nature* **335**, 740 (1988); J. Agvist, H. Luecke, F. A. Quiocho, A. Warshel, *Proc. Natl. Acad. Sci. U.S.A.* **88**, 2026 (1991); D. J. Lockhart and P. S. Kim, *Science* **257**, 947 (1992); *ibid.* **260**, 198 (1993).
19. The temperature factors for Val⁷⁶ and Gly⁷⁷ main chain atoms (but not side chain atoms) refined to higher values than for neighboring atoms. This result can be explained by the difference Fourier analysis, which shows alternative positions of the inner K^+ ion in the selectivity filter and therefore, by inference, alternative conformations of the coordinating main chain atoms, depending on the location of the K^+ ion.
20. F. Bezanilla and C. M. Armstrong, *J. Gen. Physiol.* **60**, 588 (1972).
21. B. Hille, *ibid.* **61**, 669 (1973).
22. W. Almers and E. W. McCleskey, *J. Physiol. (London)* **353**, 585 (1984); P. Hess and R. W. Tsien, *Nature* **309**, 453 (1984).
23. J. Neyton and C. Miller, *J. Gen. Physiol.* **92**, 569 (1988).
24. The KcsA gene was subcloned into pQE60 (Qiagen) vector and expressed in *E. coli* XL-1 Blue cells upon induction with 1- β -D-thiogalactopyranoside. The carboxyl-terminal histidine tagged protein was extracted by homogenization and solubilization in 40 mM decylmaltoside (Anatrace). The KcsA channel

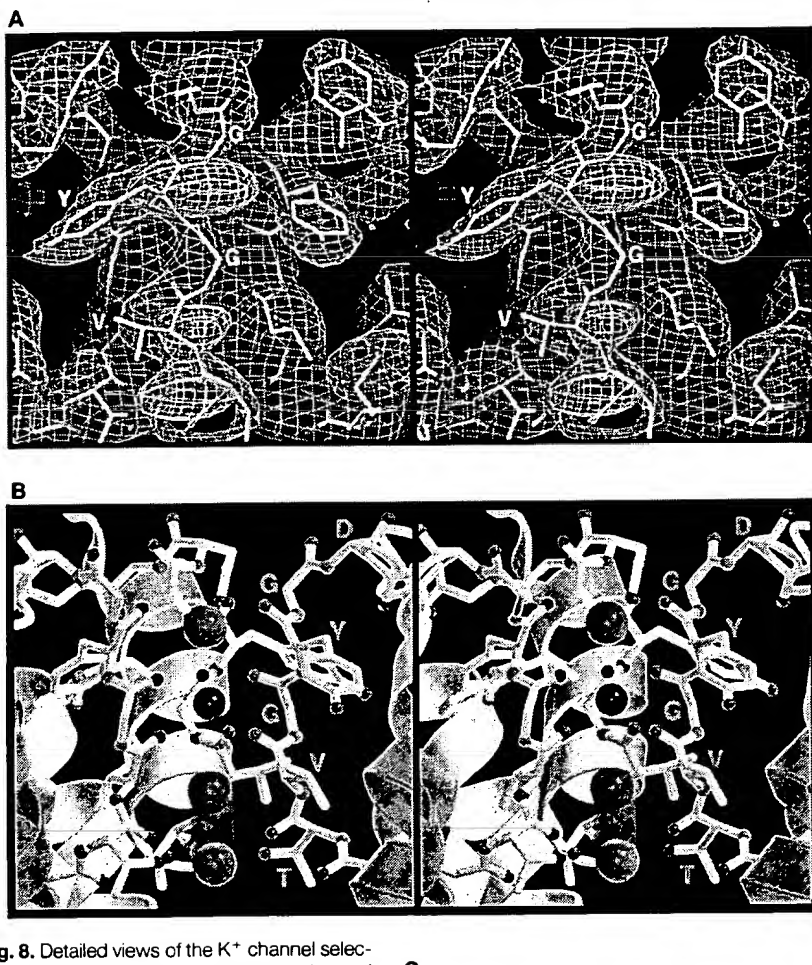


Fig. 8. Detailed views of the K^+ channel selectivity filter. (A) Stereoview of the experimental electron density (green) in the selectivity filter. The map was calculated with native-sharpened amplitudes and MIR-solvent-flattened-averaged phases. The selectivity filter of three subunits is shown as a stick representation with several signature sequence residues labeled. The Rb^+ difference map (yellow) is also shown. (B) Stereoview of the selectivity filter in a similar orientation to (A) with the chain closest to the viewer removed. The three chains represented are comprised of the signature sequence amino acids Thr, Val, Gly, Tyr, Gly running from bottom to top, as labeled in single-letter code. The Val and Tyr side chains are directed away from the ion conduction pathway, which is lined by the main chain carbonyl oxygen atoms. Two K^+ ions (green) are located at opposite ends of the selectivity filter, roughly 7.5 Å apart, with a single water molecule (red) in between. The inner ion is depicted as in rapid equilibrium between adjacent coordination sites. The filter is surrounded by inner and pore helices (white). Although not shown, the model accounts for hydrogen bonding of all amide nitrogen atoms in the selectivity filter except for that of Gly⁷⁷. (C) A section of the model perpendicular to the pore at the level of the selectivity filter and viewed from the cytoplasm. The view highlights the network of aromatic amino acids surrounding the selectivity filter. Tyrosine-78 from the selectivity filter (Y78) interacts through hydrogen bonding and van der Waals contacts with two Trp residues (W67, W68) from the pore helix.

was purified on a cobalt affinity column. Thirty-five carboxyl terminal amino acids were cleaved by chymotrypsin proteolysis. The truncated channel was purified to homogeneity by gel filtration and the detergent exchanged in a final dialysis step against 5 mM N,N-dimethyldodecylamine-N-oxide (LDAO). Crystals were grown at 20°C with the sitting drop method by mixing equal volumes of protein solution [5 to 10 mg/ml, 150 mM KCl, 50 mM Tris (pH 7.5), and 2 mM dithiothreitol] with reservoir mixture [200 mM CaCl₂, 100 mM Hepes (pH 7.5), and 48% PEG 400]. Through the entire preparation, the channel protein was maintained in solutions containing 150 mM KCl. For definition of K⁺ sites, crystals were transferred into solutions where 150 mM KCl was replaced by 150 mM RbCl or 150 mM CsCl.

25. M. W. Tate et al., *J. Appl. Crystallogr.* **28**, 196 (1995);

D. J. Thiel et al., *Rev. Sci. Instrum.* **67**, 1 (1996).

26. Z. Otwinowski, in *Data Collection and Processing*, L. Sawyer and S. Bailey, Eds. (Science and Engineering Research Council Daresbury Laboratory, Daresbury, UK, 1993), pp. 56–62.

27. Collaborative Computational Project 4 (CCP4), *Acta Crystallogr. D* **50**, 760 (1994).

28. G. M. Sheldrick, *ibid.* **46**, 467 (1990).

29. T. A. Jones, J. Y. Zou, J. Y. Cowan, M. Kjeldgaard, *ibid.* **A47**, 110 (1991).

30. A. T. Brunger, X-PLOR (Version 3.851) Manual (The Howard Hughes Medical Institute and Department of Molecular Biophysics and Biochemistry, Yale University, New Haven, CT).

31. S. J. Gamblin, D. W. Rodgers, T. Stehle, *Proceedings of the CCP4 study weekend*, Daresbury Laboratory (1996), pp. 163–169.

32. K. Y. J. Zhang and P. Main, *Acta Crystallogr.* **A46**, 377.

33. P. J. Kraulis, *J. Appl. Crystallogr.* **24**, 946 (1991).

34. O. S. Smart, J. G. Neduvellil, X. Wang, B. A. Wallace, M. P. Sansom, *J. Mol. Graphics* **14**, 354 (1996).

35. We thank D. Thiel, S. Gruner, and members of the MacCHESS staff for support and assistance in data collection at A1; J. Kuriyan, S. K. Burley, S. Harrison, P. Kim, E. Gouaux, and D. Wang for helpful discussions; Y. Jiang for help in data collection; D. Gadsby and J. Kuriyan for comments on the manuscript; and T. Rahman for patience and support. R.M. is forever grateful to T. Wiesel and A. L. MacKinnon for making this project possible. R.M. is an investigator of the Howard Hughes Medical Institute.

23 February 1998; accepted 13 March 1998

Classical Conditioning and Brain Systems: The Role of Awareness

Robert E. Clark and Larry R. Squire*

Classical conditioning of the eye-blink response, perhaps the best studied example of associative learning in vertebrates, is relatively automatic and reflexive, and with the standard procedure (simple delay conditioning), it is intact in animals with hippocampal lesions. In delay conditioning, a tone [the conditioned stimulus (CS)] is presented just before an air puff to the eye [the unconditioned stimulus (US)]. The US is then presented, and the two stimuli coterminate. In trace conditioning, a variant of the standard paradigm, a short interval (500 to 1000 ms) is interposed between the offset of the CS and the onset of the US. Animals with hippocampal lesions fail to acquire trace conditioning. Amnesic patients with damage to the hippocampal formation and normal volunteers were tested on two versions of delay conditioning and two versions of trace conditioning and then assessed for the extent to which they became aware of the temporal relationship between the CS and the US. Amnesic patients acquired delay conditioning at a normal rate but failed to acquire trace conditioning. For normal volunteers, awareness was unrelated to successful delay conditioning but was a prerequisite for successful trace conditioning. Trace conditioning is hippocampus dependent because, as in other tasks of declarative memory, conscious knowledge must be acquired across the training session. Trace conditioning may provide a means for studying awareness in nonhuman animals, in the context of current ideas about multiple memory systems and the function of the hippocampus.

Memory is composed of several different abilities that depend on different brain systems (1). A fundamental distinction is between the capacity for conscious recollection of facts and events (declarative or explicit memory) and various nondeclarative (implicit) forms of memory that are expressed in skills, habits, and simple forms of conditioning. This distinction is dramatically evident in amnesic patients, who have bilateral damage to the hippocampal formation or related midline diencephalic brain structures. These patients have severely im-

paired declarative memory and are profoundly forgetful. Yet these same patients have a fully intact capacity for nondeclarative memory (2). Indeed, a large body of literature involving both humans and experimental animals can now be understood by recognizing that memory tasks requiring declarative memory depend on the integrity of the hippocampal formation and related structures, whereas tasks requiring nondeclarative memory can be performed normally after damage to these structures and are supported by other brain systems. Declarative memory is what is meant by the term "memory" in ordinary language. It is involved in modeling the external world, and its contents can be brought to consciousness as a verbal proposition or as a mental image. By contrast, nondeclarative memory is expressed through performance

without affording access to any conscious memory content or even awareness that memory is being used. This form of memory permits cumulative changes in perceptual and response systems and allows for the gradual development of new skills and habits.

A major puzzle about the distinction between conscious (hippocampus dependent) and nonconscious (hippocampus independent) forms of memory concerns classical conditioning. Classical conditioning, a phylogenetically early example of simple associative learning, has been studied extensively and would appear to be a quintessential example of nondeclarative memory (3). In perhaps the best studied classical conditioning paradigm, delay conditioning of the eye-blink response, a neutral conditioned stimulus (CS), such as a tone, is presented just before an air puff unconditioned stimulus (US). The US is then presented and the two stimuli coterminate (Fig. 1, A and B). Initially, an eye blink occurs reflexively in response to the US, but with repeated CS-US pairings a learned or conditioned response (CR) is elicited by the CS in advance of the US. The CR overlaps with the US such that the eye blink serves as an adaptive, defensive response to the air puff. Studies in the rabbit have shown that the cerebellum is essential for both the acquisition and retention of delay classical conditioning (4) and that no other forebrain structure, including the hippocampus, is required (5). Amnesic patients also exhibit intact acquisition and retention of the classically conditioned eye-blink response (6, 7). Thus, eye-blink conditioning appears to have the automatic, reflexive features that are characteristic of nondeclarative memory.

The puzzle concerns trace conditioning, a slightly different version of classical conditioning in which the CS is presented and terminated and then a short interval is imposed before the presentation of the US (8) (Fig. 1, C and D). The name comes from the fact that the CS must leave some trace in the nervous system for a CS-US associ-

R. E. Clark is in the Department of Psychiatry, University of California, San Diego, La Jolla, CA 92093, USA. L. R. Squire is at the Veterans Affairs Medical Center, San Diego, CA 92161, USA, and Departments of Psychiatry and Neurosciences, University of California, San Diego, School of Medicine, La Jolla, CA 92093, USA.

*To whom correspondence should be addressed.

**This Page is Inserted by IFW Indexing and Scanning
Operations and is not part of the Official Record**

BEST AVAILABLE IMAGES

Defective images within this document are accurate representations of the original documents submitted by the applicant.

Defects in the images include but are not limited to the items checked:

- ☐ BLACK BORDERS
- ☐ IMAGE CUT OFF AT TOP, BOTTOM OR SIDES
- ☒ FADED TEXT OR DRAWING
- ☐ BLURRED OR ILLEGIBLE TEXT OR DRAWING
- ☐ SKEWED/SLANTED IMAGES
- ☐ COLOR OR BLACK AND WHITE PHOTOGRAPHS
- ☐ GRAY SCALE DOCUMENTS
- ☐ LINES OR MARKS ON ORIGINAL DOCUMENT
- ☐ REFERENCE(S) OR EXHIBIT(S) SUBMITTED ARE POOR QUALITY
- ☐ OTHER: _____

IMAGES ARE BEST AVAILABLE COPY.

As rescanning these documents will not correct the image problems checked, please do not report these problems to the IFW Image Problem Mailbox.